

Full on-device manipulation of olefin metathesis for precise manufacturing

Received: 25 May 2024

Accepted: 26 September 2024

Published online: 8 November 2024

 Check for updates

Yilin Guo^{1,8}, Chen Yang^{1,8}, Lei Zhang^{1,8}, Yujie Hu², Jie Hao³, Chuancheng Jia³, Yang Yang⁴, Yan Xu¹, Xingxing Li², Fanyang Mo⁵, Yanwei Li⁶, Kendall N. Houk⁷ & Xuefeng Guo^{1,3}

Olefin metathesis, as a powerful metal-catalysed carbon–carbon bond-forming method, has achieved considerable progress in recent years. However, the complexity originating from multicomponent interactions has long impeded a complete mechanistic understanding of olefin metathesis, which hampers further optimization of the reaction. Here, we clarify both productive and hidden degenerate pathways of ring-closing metathesis by focusing on one individual catalyst, using a sensitive single-molecule electrical detection platform. In addition to visualizing the full pathway, we found that the conventionally unwanted degenerate pathways have an unexpected constructive coupling effect on the productive pathway, and both types of pathway can be regulated by an external electric field. We then pushed forward this ability to ring-opening metathesis polymerization involving more interactive components. With single-monomer-insertion-event resolution, precise on-device synthesis of a single polymer was achieved by online manipulation of monomer insertion dynamics, intramolecular chain transfer, stereoregularity, degree of polymerization and block copolymerization. These results offer a comprehensive mechanistic understanding of olefin metathesis, exemplifying infinite opportunities for practical precise manufacturing.

Olefin metathesis is a versatile method for synthesizing diverse olefins via C=C double-bond reorganization^{1–4}, with widespread applications in organic synthesis^{5–8} and polymer synthesis^{7,9–11}. Previously, the combination of rational catalyst design and traditional macroscopic analytical techniques accelerated the understanding and optimization of the olefin metathesis process. In particular, a series of organometallic catalysts based on N-heterocyclic carbene ligands has been developed to improve the catalytic efficiency, stability and selectivity¹². However, several

critical issues still remain unaddressed: for example, (1) the real-time trajectory of the catalytic cycle is unknown, and the catalyst activity does not account for non-productive metathesis events; (2) the polymerization dynamics is inaccessible with single-monomer-insertion precision; (3) a universal strategy for achieving Z-selective olefin metathesis and controlling the degree of polymerization (DP) is urgently needed.

Extensive efforts have been made to address these challenges. Non-productive metathesis has been studied by using

¹Beijing National Laboratory for Molecular Sciences, National Biomedical Imaging Centre, College of Chemistry and Molecular Engineering, Peking University, Beijing, People's Republic of China. ²Department of Chemical Physics, University of Science and Technology of China, Hefei, People's Republic of China. ³Centre of Single-Molecule Sciences, Institute of Modern Optics, Frontiers Science Centre for New Organic Matter, College of Electronic Information and Optical Engineering, Nankai University, Tianjin, People's Republic of China. ⁴Department of Chemistry and Biochemistry, University of California, Santa Barbara, CA, USA. ⁵School of Materials Science and Engineering, Peking University, Beijing, People's Republic of China. ⁶Environment Research Institute, Shandong University, Qingdao, People's Republic of China. ⁷Department of Chemistry and Biochemistry, University of California, Los Angeles, Los Angeles, CA, USA. ⁸These authors contributed equally: Yilin Guo, Chen Yang, Lei Zhang. ✉ e-mail: fmo@pku.edu.cn; lyw@sdu.edu.cn; houk@chem.ucla.edu; guoxf@pku.edu.cn

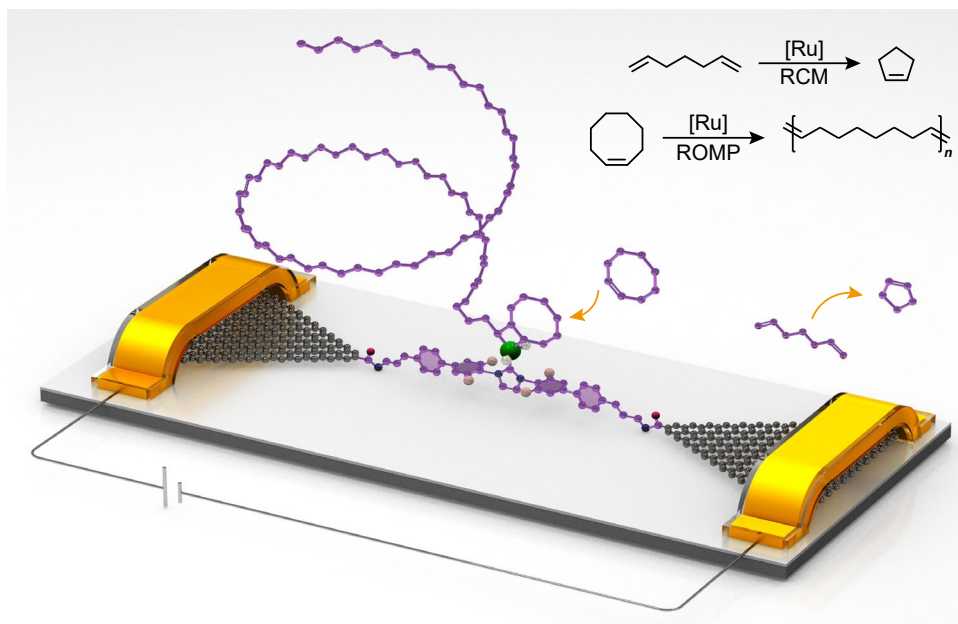


Fig. 1 | Schematic of a single-catalyst junction focusing on RCM and ROMP. Hydrogen atoms are omitted for clarity.

deuterium-labelled olefins; this enables quantitative analysis of productive and degenerate metathesis reactions^{13–15}. However, a more complete picture of the catalyst efficiency awaits further elucidation. Regarding the polymerization dynamics of ring-opening metathesis polymerization (ROMP), researchers have focused on reducing the dimensionality of polymers to the single-polymer-aggregate^{16–18} or even single-catalyst¹⁹ level. However, the sensitivities of current characterization methods are not high enough to detect real-time single-insertion events, necessitating single-catalyst and single-monomer-insertion-event resolution. Highly selective kinetic generation of *Z*-olefins has been achieved because of advances in stereocontrolled olefin metathesis with tungsten, molybdenum and ruthenium catalysts^{20–29}. Even so, developing new universal approaches that offer facile access to stereoselective metathesis for a range of substrates and reaction classes remains crucial.

To this end, focusing on only one molecule—for example, trapping a catalyst by integration into electrodes—might enable us to decipher detailed thermodynamic and kinetic information on catalytic reactions with single-molecule and single-event resolution, which should be a promising strategy for addressing all the above challenges. Such single-molecule detection techniques have proved their feasibility and reliability in unveiling the intrinsic properties of reactions. Real-time monitoring of conductance variations synchronously reflects the structural changes in the reaction active site, which affords the ability to visualize reaction trajectories^{30–33}, capture short-lived (microsecond-to millisecond-scale) intermediates^{34–36} and describe the interaction networks among components^{37,38}. In this study, graphene–molecule–graphene single-molecule junctions are adopted as the tool to investigate olefin metathesis owing to the determined molecule–electrode interface coupling, good tolerance to chemical treatments and external stimuli, and high spatiotemporal resolutions^{39,40}.

In this Article, we construct a single-catalyst junction and focus on two types of olefin metathesis: ring-closing metathesis (RCM) and ROMP (Fig. 1). Real-time single-molecule electrical spectroscopy with high time resolution enables the visualization of reaction trajectories, demonstrating the hidden degenerate pathways in RCM and intramolecular backbiting in ROMP. In addition, with external electric fields (EEFs), we achieve precise online manipulation of monomer insertion dynamics, intramolecular chain transfer, stereoselectivity, DP and block copolymerization.

Device fabrication and characterization

The dashed-line lithographic technique⁴¹ was used to prepare nanogapped and carboxyl-terminal graphene point electrode arrays on a SiO₂/Si chip via electron-beam lithography and oxygen plasma etching. We integrated a molecular bridge, which contains a second-generation Hoveyda–Grubbs catalyst (HG2) centre with azido-functionalized end groups, into the electrode pairs by formation of amide bonds. Details of the procedures for molecular synthesis are provided in Supplementary Section 1, Supplementary Scheme 1. Details of device fabrication and characterization can be found in Methods. In comparison with the lack of current response to applied bias voltages in the open-circuit state before molecular incorporation, the recovered current–voltage (*I*–*V*) response indicates successful connection of the molecular bridge. About 16 of 72 devices on the same chip showed *I*–*V* responses under optimized conditions (Supplementary Section 2, Supplementary Fig. 1), which reached a connection yield of ~22%. Statistical analysis (Supplementary Section 3) showed that the probability of electrical signals originating from only one molecular connection between electrode pairs is ~90%.

Deciphering degenerate pathways in RCM

RCM has been extensively used in synthetic chemistry to construct functionalized cyclic systems⁴². Yet, [2 + 2]-cyclization among multi-component olefin groups brings the emergence of complexity^{43,44}, and thus non-productive (degenerate) pathways (such as those mentioned in Fig. 2a). Elegant approaches for characterizing non-productive metathesis reactions have been established via isotope-labelling experiments¹⁵, revealing kinetic information for productive and degenerate processes. Nonetheless, data for metathesis between both labelled or both unlabelled substrates cannot be obtained (same product as substrate), necessitating real-time in situ monitoring and single-molecule resolution.

Diethyl diallylmalonate is one of the standard substrates used for comparing and evaluating metathesis catalysts in RCM¹². We explored the RCM of diethyl diallylmalonate with the catalysis of single-HG2 junctions. A bias voltage of 300 mV was applied to the single-catalyst junction and the electrical signal was recorded at a sampling rate of 57.6 kHz. The catalyst was preactivated to a Ru-based methylenide complex as the initial state **1** (–22.5 nA) under an ethylene atmosphere (Supplementary Fig. 2). Diethyl diallylmalonate (1×10^{-6} mol l⁻¹) in

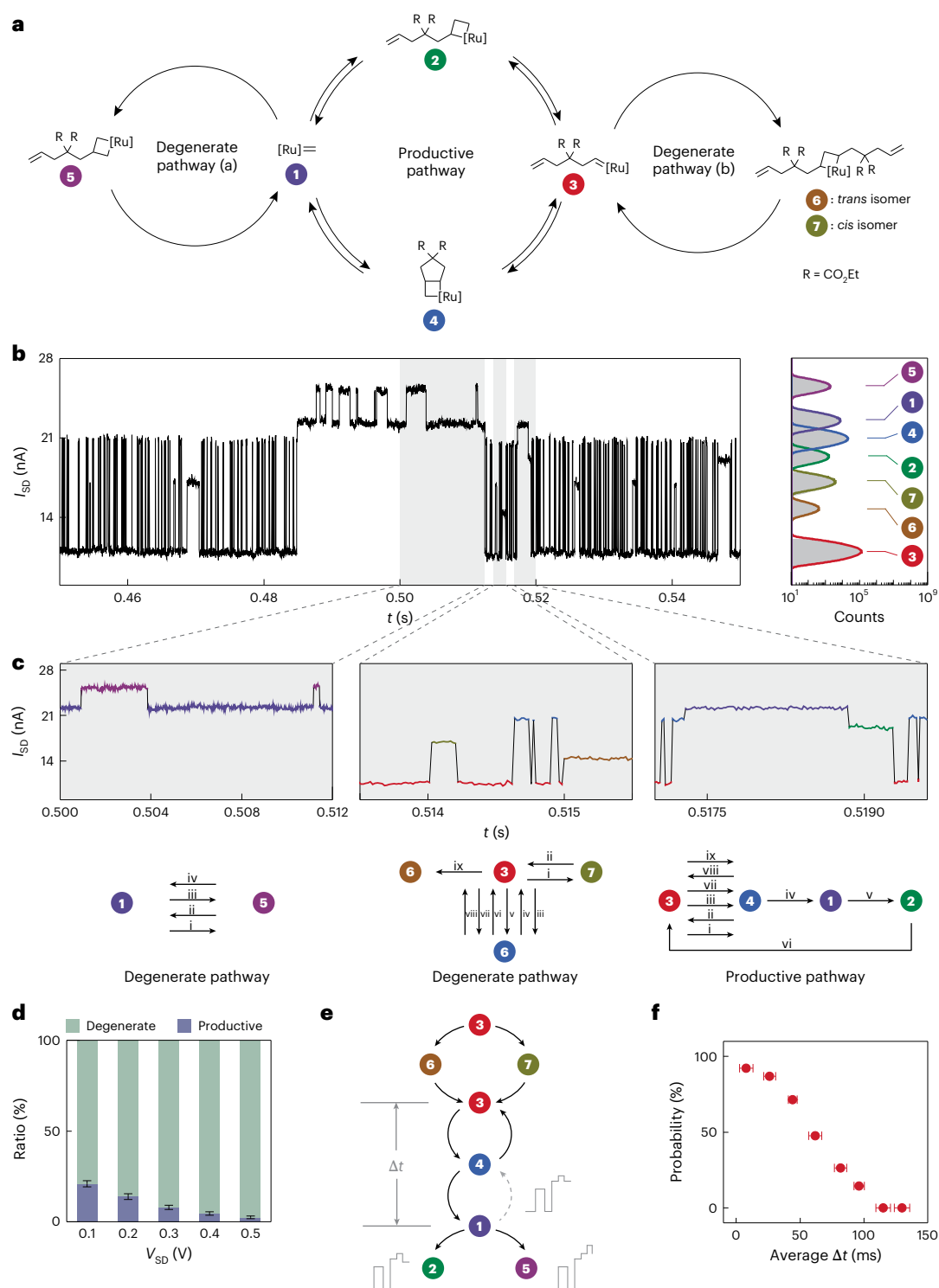


Fig. 2 | Electrical characterization and signal assignment for RCM at single-catalyst junctions. **a**, Measurable pathways in the RCM of diethyl diallylmalonate, including one productive and two degenerate pathways. **b**, Recorded $I-t$ curve of reactions, corresponding histograms and assignment of seven conductance states at $V_{SD} = 0.3$ V. The complexes with conductance from low to high are ruthenium alkylidene (3), *trans*- α , α -disubstituted metallacyclobutane (6), *cis*- α , α -disubstituted metallacyclobutane (7), α -substituted metallacyclobutane (2), α , β -disubstituted metallacyclobutane (4), ruthenium methylidene (1) and β -substituted metallacyclobutane (5). I_{SD} , source-drain current. **c**, Three typical reaction trajectories of productive and degenerate pathways, and corresponding transition relationships between intermediates. The Roman numbers show the transition sequences from left to right. **d**, Ratios of NOEs of productive and degenerate pathways under different

positive bias voltages. The error scales were derived from the statistics of ten independent tests on the same device ($n = 10$) (Supplementary Figs. 16–25). Data are presented as mean \pm s.d. **e**, Conversion networks of degenerate coupled productive pathways. The three idealized $I-t$ curves correspond to three conversion relationships: 3 \rightarrow 6 (7) \rightarrow 3 \rightarrow 4 \rightarrow 1 \rightarrow 2; 3 \rightarrow 6 (7) \rightarrow 3 \rightarrow 4 \rightarrow 1 \rightarrow 5; 3 \rightarrow 6 (7) \rightarrow 3 \rightarrow 4 \rightarrow 1 \rightarrow 4. **f**, Plot of probability versus average Δt . Probability = (number of samples generating product)/(sum of samples); Δt is the time interval between 3 and 1, as shown in e. Statistics are derived from 206 independent time sequences of electrical signals measured from the same device. The distribution of Δt is shown as a scatter plot, depicting the mean value and s.d. The number of time sequences in each time interval is as follows: $n_{7.9\text{ms}} = 78$, $n_{26.2\text{ms}} = 54$, $n_{44.1\text{ms}} = 21$, $n_{61.9\text{ms}} = 21$, $n_{81.8\text{ms}} = 19$, $n_{96.2\text{ms}} = 7$, $n_{115.2\text{ms}} = 3$ and $n_{129.8\text{ms}} = 3$ (the subscript refers to the mean value of Δt).

toluene was added to the laboratory-built reaction cell containing the molecular bridge at complex **1**. The recorded RCM current–time ($I-t$) curve (Fig. 2b) indicates the interconversions among seven conductance states (the long-term $I-t$ curves are provided in Supplementary Fig. 3). A series of intermediate-controlled experiments (Supplementary Section 6, Supplementary Figs. 4–7), inelastic electron tunnelling spectra (Supplementary Figs. 8 and 9), simulated potential energy profiles (Extended Data Fig. 1) and electron transmission spectra (Supplementary Fig. 10) provided the assignments of all the conductance states. These assignments presented a network consisting of one productive and two degenerate conversion pathways (Fig. 2a), providing a clear insight into the mechanism of olefin metathesis. Note that the other, unmeasurable, degenerate pathway (c) (Supplementary Scheme 2) was not energy preferred according to computational studies (Extended Data Fig. 1d).

Specifically, in the productive pathway, the association of the substrate and a ruthenium methyldiene complex (**1**) leads to the formation of α -substituted metallacyclobutane (**2**), which subsequently undergoes [2 + 2]-cycloreversion to release ethylene and a new ruthenium alkylidene (**3**). Complex **3** is then converted to a new metallacyclobutane (**4**) via intramolecular cycloaddition, and retro-cycloaddition furnishes the product cyclopentene. In degenerate pathway (a), β -substituted metallacyclobutane (**5**) is produced via a different olefin-binding configuration (in comparison with the conversion from **1** to **2**), and reproduces the initial methyldiene **1** and the starting substrate. Similarly, α , α -disubstituted metallacyclobutane (*trans* isomer **6**; *cis* isomer **7**) is generated by coordination of the substrate with alkylidene **3** (degenerate pathway (b)). Figure 2c shows three typical reaction trajectories of the productive and degenerate pathways, providing the real-time transition relationship and detailed dynamic information. More importantly, it enables accurate statistics on the number of events (NOE), providing a quantitative description of unclear degenerate pathways (Supplementary Fig. 11). Specifically, the exchange of the terminal carbon between two olefins was determined to be the dominant degenerate pathway, especially via a *cis* metallacyclobutane, **7** (NOE > 20 at 0.1 V, Supplementary Fig. 11). The exchange of the terminal carbon between olefins and complex **1** was also obtained and no coupling between two olefins was detected.

It is worth mentioning that the regulation of the reaction by the EEF cannot be neglected^{34,45–49}. Bias-voltage-dependent measurements (including positive and negative biases) were reproducibly conducted to analyse the impact of the EEF on the productive/degenerate pathways (Supplementary Figs. 12–24). Except for the transition from **3** to **7** (degenerate), the NOE (**4** \rightarrow **1**, productive; **1** \rightarrow **5**, degenerate; **3** \rightarrow **6**, degenerate) showed a decreasing trend. The ratio of productive events gradually declined with increasing voltage (positive bias, Fig. 2d; negative bias, Supplementary Fig. 25), which implies that the EEF inhibits productive metathesis. Computational studies showed that the energy barrier rises more notably for the productive pathway than for the degenerate pathway (Supplementary Table 1). This suggests that the adopted EEF could potentially achieve online manipulation of olefin metathesis (see below).

Conventionally, the degenerate pathways are regarded as unwanted work of the catalyst, which reduce the opportunities for productive metathesis. However, a long-term statistical analysis showed that the degenerate and productive pathways have a strong correlation in some cases. As shown in Fig. 2e, degenerate pathway (b) (**3** \rightarrow **6** \rightarrow **3**; **3** \rightarrow **7** \rightarrow **3**) followed by **4** and **1** involves three forks. Forks **1** \rightarrow **2** and **1** \rightarrow **5** lead to successful release of the product cyclopentene. The third fork, that is, **1** \rightarrow **4**, represents a reversible process and does not generate products. In the electrical experiment of RCM (substrate concentration 1×10^{-10} mol l⁻¹), we extracted current signals (sample size 206; typical $I-t$ curves are provided in Supplementary Fig. 26) involving the species conversion modes in Fig. 2e, and recorded the time interval (Δt) between **3** (after **6** or **7**) and **1**, and the corresponding fork (**1** \rightarrow **2**,

1 \rightarrow **5** or **1** \rightarrow **4**). A plot of the probability of generating products versus Δt shows an obvious anticorrelation trend (Fig. 2f), demonstrating that in the case of a short Δt degenerate pathway (b) would promote an entry of Ru-based methyldiene **1** into the next catalytic process and product release (for example, for $\Delta t \approx 7.89 \pm 5.22$ ms, the probability is up to $\sim 92.3\%$). This may arise from the presence of diethyl diallylmalonate (substrate or the product of degenerate pathway (b)) around the catalytic centre, which inhibits the reversible conversions between **1** and **4**, and favours product formation. As Δt increases, the probability that diethyl diallylmalonate involved in degenerate pathway (b) escapes from the solvent cage increases, which weakens the constructive coupling effect on the productive pathway.

Manipulating backbiting in ROMP

In most cases, cyclic oligomers are undesired by-products originating from intramolecular backbiting in ROMP (Fig. 3a). The ring–chain equilibrium (polymerization and cyclodepolymerization) is highly dependent on the monomer concentration, favouring linear polymer chains in high concentrations and cyclic oligomers in high dilutions⁵⁰. Nevertheless, cyclic oligomers are to some extent still present in a high-concentration system, highlighting the need to develop efficient approaches to completely inhibit their generation.

With cyclooctene (COE) (1×10^{-4} mol l⁻¹) in toluene, we first characterized the electrical signals of single-polymer-chain growth at 0.1 V. Binary switching shows a rising square shape in the initial stage (0–42 s) and subsequent stabilization (Fig. 3b). The RCM results suggest that the electrical signals can be attributed to the alternating transformation of ruthenium alkylidene and metallacyclobutane with increasing DP. The polymer chain length affects the conductance to some extent when $DP \leq 10$ (grey shaded region in Fig. 3b), leading to gradually ascending square signals. Further extension of the chain ($DP > 10$) does not affect the conductance because of the molecular orbitals of the polymer chain outside the electron transmission channel. Importantly, one square-like signal represents a monomer-insertion process, which affords single-monomer-insertion-event resolution. An abrupt current decrease implies the shortening of the polymer chain—that is, backbiting occurs (marked by arrows in Fig. 3b). Because there is only one catalyst in the system, intermolecular chain transfer can be excluded as the cause of depolymerization.

Optical characterization further supported polymerization and cyclodepolymerization. The catalyst terminus was modified with a fluorescent polystyrene bead to enable fluorescent tracking of the trajectory of the polymer chain end during propagation (Fig. 3c and Supplementary Video 1; the modification procedures are described in Methods). Three different trajectories (right-hand panel in Fig. 3d) correspond to different time periods (marked by strips in the $I-t$ curve in the left-hand panel in Fig. 3d) with different ranges of motion. The range of motion of the yellow trajectory is smaller than that of the blue trajectory, implying a decreased chain length. In other words, backbiting occurred before the time point marked by the yellow strip. The electrical signal, that is, a sharp drop in the current level, also supports this observation. The optical and electrical signals consistently support the phenomena of polymerization and backbiting at the single-catalyst site.

The effects of the EEF on polymerization/cyclodepolymerization were investigated through bias-voltage-dependent measurements (Fig. 3e and Supplementary Fig. 27). The results show that the EEF has a suppression effect on the backbiting behaviour. Owing to the ~ 500 pA current resolution, we can distinguish the conductance at $DP \leq 10$ at present. Therefore, only a backbiting process generating new ruthenium alkylidene at $DP \leq 10$ can be observed directly via the abrupt decrease in current levels. Note that another type of intramolecular backbiting, which does not alter polymer chain lengths, also exists (Supplementary Fig. 28). Although not all of the backbiting processes can be monitored, the trend in the measurable region reflects the

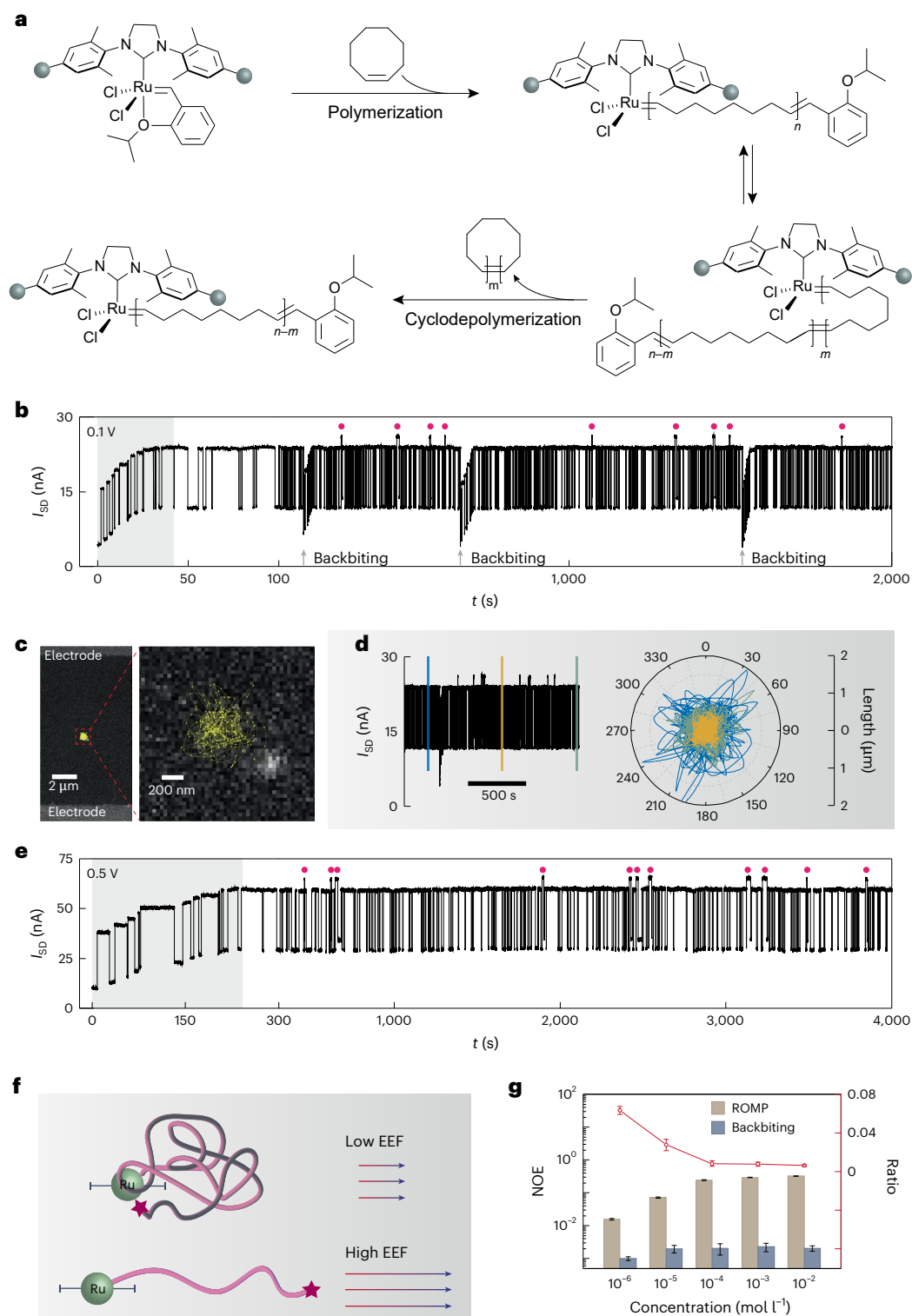


Fig. 3 | Manipulation of backbiting in ROMP. **a**, Schematic of polymerization and cyclo-depolymerization (backbiting) in ROMP. **b**, $I-t$ curve of single-polymer-chain growth under a bias voltage of 0.1 V (COE concentration $1 \times 10^{-4} \text{ mol l}^{-1}$). Time points of backbiting are marked with arrows. The occasional current increases (marked by red dots) during polymerizations refer to the Z-isomer (see below). For clarity, the x axis in the ranges of 0–100 s and 100–2,000 s adopts different time scales. **c**, Fluorescent imaging of polymer chain terminus in the propagation process, showing the trajectories of the polymer chain end (yellow curves). The bright pixels refer to the fluorescent polystyrene bead at that moment. The small yellow dots are centroids of the fluorescent region at different times, showing the trajectory of the polymer chain end. A 405 nm, 5 mW laser was focused on the graphene device through a $\times 100$ oil lens with an

exposure time of 50 ms. **d**, Part of the $I-t$ curve in ROMP, and the corresponding three trajectories (each ~ 21 s during the time period indicated by the strip width) of the polymer chain end. **e**, $I-t$ curve of single-polymer-chain growth under a bias voltage of 0.5 V (COE concentration $1 \times 10^{-4} \text{ mol l}^{-1}$). For clarity, the x axis in the ranges of 0–300 s and 300–4,000 s adopts different time scales. **f**, Schematic of conformation stretching of polymer chain under the increased EEF. **g**, Plots of NOE versus COE concentration (bar charts refer to left y axis), and ratios of NOE (backbiting)/NOE (polymerization) versus COE concentration (line charts refer to right y axis) in monomer-concentration-dependent measurements ($V_{sp} = 0.1 \text{ V}$). The error scales were derived from the statistics of ten different devices ($n = 10$). Data are presented as mean \pm s.d.

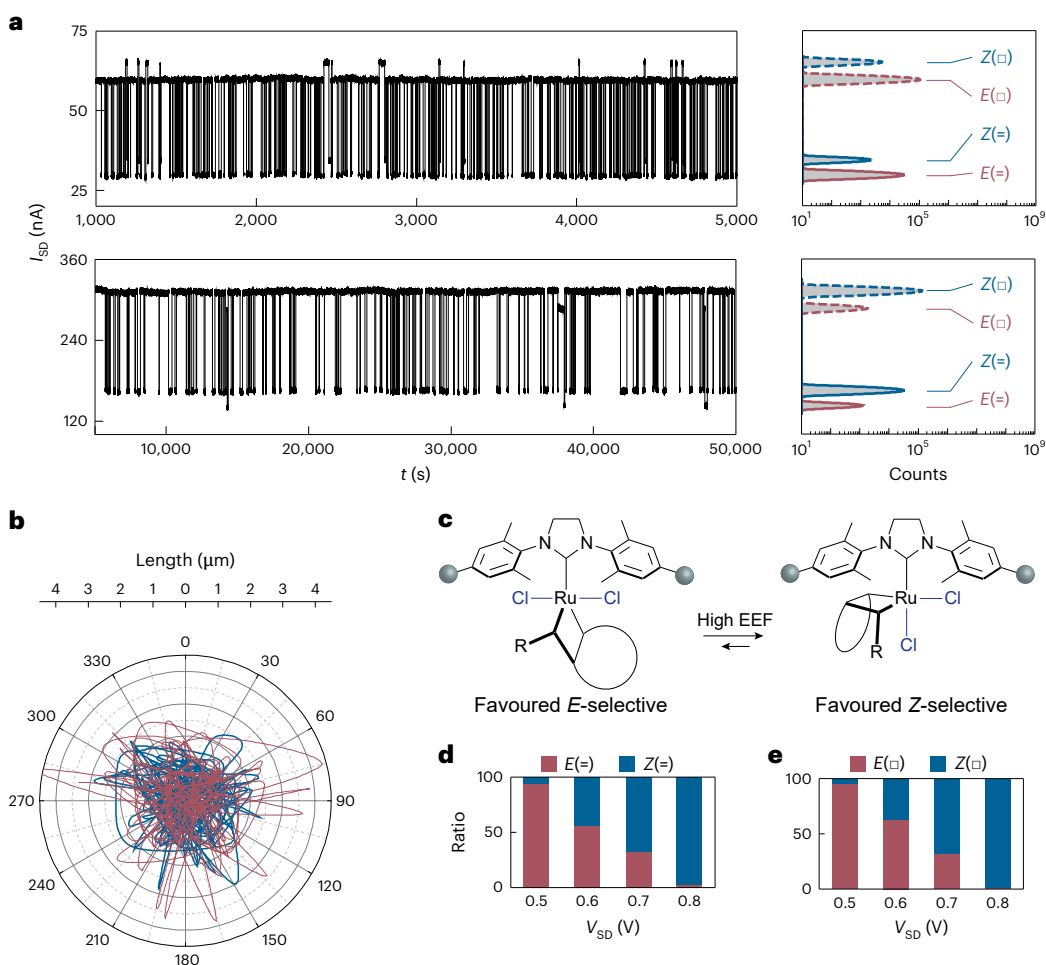


Fig. 4 | Stereo control of ROMP. **a**, I - t curves of single-polymer-chain growth under a bias voltage of 0.5 V (top panel) and 0.8 V (bottom panel), and the corresponding histograms. □, Ru-based metallacyclobutane; =, Ru-based alkylidene. **b**, Two trajectories (same counted DP) of polymer chain ends

dominated by E (red) or Z (blue) units. **c**, Proposed isomerization of HG2 in a high EEF. **d**, Ratios of $E(=)$ and $Z(=)$ versus bias voltages. **e**, Ratios of $E(\square)$ and $Z(\square)$ versus bias voltages.

suppression effect. In addition, as a benefit of single-event resolution, the monitored electrical signal also demonstrates the dynamic disorder of olefin metathesis, that is, the dynamic effect of the chain conformation on the reaction (Supplementary Figs. 29 and 30).

The impact of the EEF on backbiting results from its pulling force on the isopropoxyaryl terminus of the polymer chain. In the absence of an EEF or at low EEFs, a conformationally entangled ‘hairball’⁴⁹ wraps around the catalyst (Fig. 3f), which increases the probability of intramolecular chain transfer. In contrast, the interaction between a high EEF and the polar terminal group contributes to the stretching conformation of the polymer chain (Fig. 3f), which reduces the chance of the catalyst centre coordinating with the polymer backbone. This explanation is supported by controlled experiments (Supplementary Fig. 31) with a non-polar-terminus chain (vinyl group). Therefore, the EEF acts as a comb, which can unravel the entangled polymer chain and thereby inhibit backbiting. Regulation of the chain conformation and polymerization dynamics enables online precise (by-product-free) synthesis with single-molecule resolution.

The sensitivity of polymerization/cyclodepolymerization to monomer concentration was verified through monomer-concentration-dependent measurements. Ten devices were independently tested at source–drain voltage (V_{SD}) = 0.1 V; the average results are shown in Fig. 3g (long-term I - t curves are provided in Supplementary Figs. 32–41). Benefiting from the capability of direct detection of monomer insertion in real time, the detailed dynamic parameters of

an individual catalyst can be obtained. The NOE per second reflects the monomer-insertion rate: for example, at a COE concentration of $1 \times 10^{-2} \text{ mol l}^{-1}$, $\text{NOE}(\text{ROMP}) = 0.3267 \pm 0.0048 \text{ s}^{-1}$ and $\text{NOE}(\text{backbiting}) = 0.0021 \pm 0.0004 \text{ s}^{-1}$. The $\text{NOE}(\text{backbiting})$ to $\text{NOE}(\text{ROMP})$ ratio decreased with increasing concentration, which is consistent with the ensemble experiments, and proves the reliability of the platform. In addition, two kinds of monomer, COE and norbornene (NBE), were subjected to bias-voltage-dependent measurements of single-catalyst polymerization to determine more specific dynamic information. Statistical results are provided in Extended Data Fig. 2.

Controlling stereoselectivity in ROMP

In addition to the monomer-insertion rate, the configuration of each insertion event can also be distinguished via electrical signals. As shown in Fig. 3b, E -ruthenium-alkylidene (-11.8 nA) and E -metallacyclobutane (-24.0 nA) are predominant, while Z -ruthenium-alkylidene (-13.9 nA) and Z -metallacyclobutane (-26.1 nA) are occasionally observed. Control experiments, of in situ preparation of the Z -selective polymer with the assistance of bidentate ligands and in situ ligand exchange, support these assignments (Supplementary Figs. 42 and 43). This reflects the preference of HG2 for the formation of thermodynamically favoured E -olefins. Inspired by this, the EEF was applied to force the two Cl ligands to adopt a *syn* orientation. With increasing biases from 0.5 to 0.8 V, the $Z:E$ ratios underwent a notable reversal (Fig. 4a), that is, HG2 in a high EEF (0.8 V) favours Z -selectivity (electrical signals at 0.6 and 0.7 V are

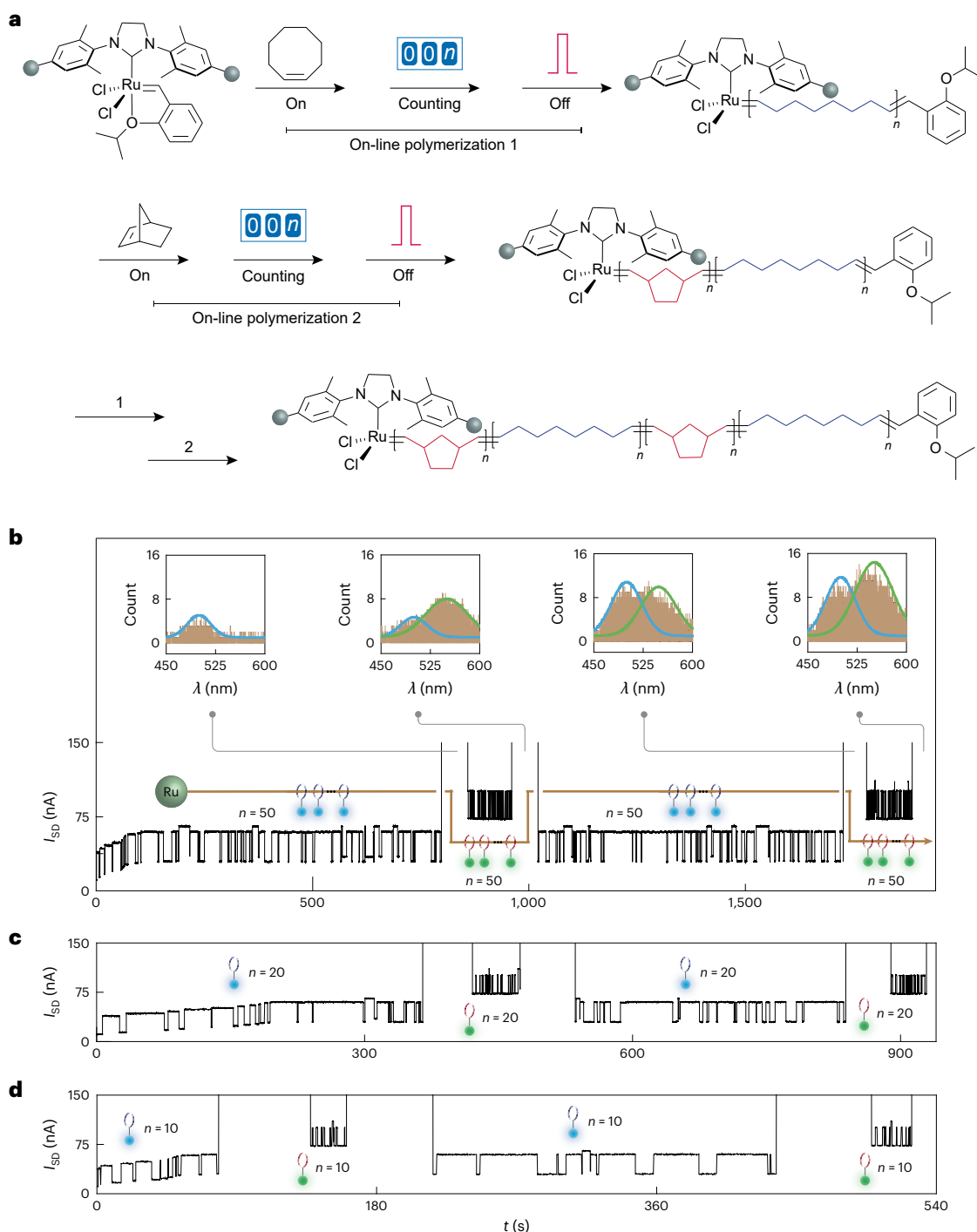


Fig. 5 | Precise synthesis of block copolymers. **a**, Schematic of online synthesis of block copolymers. **b**, I - t curve ($n = 50$) under the operations $1 \rightarrow 2 \rightarrow 1 \rightarrow 2$, and histograms of recorded emitted photons at different time points; n is the number of repeated units in each segment. The ball emitting blue light

represents f-COE and the green one represents f-NBE. λ , wavelength. **c**, I - t curve of the copolymerization process with $n = 20$. **d**, I - t curve of the copolymerization process with $n = 10$.

provided in Supplementary Fig. 44). The two trajectories of polymer chain ends dominated by *E* (red) or *Z* (blue) units show a wider range of motion for the *E*-selective chain (Fig. 4b), which further supports the assignments of the isomers.

Specifically, the *Z*-selectivity in a high EEF can be attributed to the stabilization effect of the high electric field on the dipole complex. Due to the electronic repulsion between the axially and equatorially situated *syn* Cl ligands, the dichloro-ruthenium catalyst adopts the *anti* configuration (Fig. 4c, left) in the absence of an EEF or at low EEFs,

leading to the predominant generation of *E*-products. However, the high dipole moment of the *syn* Cl ligands is stabilized at high EEFs, thereby mainly delivering *Z*-olefins (Fig. 4c, right). Computational simulation (Supplementary Fig. 45) demonstrates that the energy of the *syn* configuration decreases with increasing EEF, which supports the above scenario. As shown in Supplementary Fig. 46, the *E*-isomer with *anti* Cl ligands is more energy preferred than the *Z*-isomer with *anti* Cl ligands under arbitrary EEF strengths, which excludes the possibility of the predominance of *anti*-Cl-*Z*-isomer at high EEFs. Statistical

results (Fig. 4d,e) show that the *Z:E* ratios of ruthenium-alkylidene and metallacyclobutane complexes reached ~97:3 and ~96:4 ($V_{SD} = 0.8$ V), respectively, indicating the high efficiency and stereoselectivity of this approach.

Precise synthesis of block copolymers

As the bias voltage was further increased, we found that polymerization stopped at $V_{SD} = 1$ V (Supplementary Fig. 47), consistent with the computational EEF-dependent reactivity. This provides an alternative method for terminating ROMP. More importantly, this strategy facilitates the precise synthesis (one-monomer resolution) of polymer with desired DP and the sequence-controlled copolymer as depicted in Fig. 5a. Initially, COE undergoes homoaddition n times at $V_{SD} = 0.5$ V (n is the desired number of repeated units), and then polymerization is immediately terminated by increasing V_{SD} to 1 V (operation 1). Then, we remove the COE solution and add the comonomer, namely, NBE, to perform a similar operation (operation 2). Finally, a sequence-controlled copolymer is obtained by repeating these two operations.

To better characterize the copolymerization, fluorescent-group-substituted COEs (f-COEs) and NBEs (f-NBEs) are selected as the comonomers (detailed molecular synthesis is provided in Supplementary Section 1). Figure 5b displays the $I-t$ curve for operations $1 \rightarrow 2 \rightarrow 1 \rightarrow 2$ and histograms of the recorded emitted photons at different time points. The single-monomer-insertion-event resolution enables real-time counting and control of the DP. After counting the number of incorporated f-COEs ($n = 50$), we applied a voltage of 1 V to turn off the polymerization and removed the substrates. We then recorded the fluorescence spectrum of the homopolymerized segment of f-COEs at the single-catalyst site (the first histogram in Fig. 5b). The emission peak is centred at ~500 nm, which is consistent with the macroscopic spectrum of the f-COEs (Supplementary Fig. 48). This shows that olefin metathesis proceeded smoothly, and that the monomer was successfully incorporated. Similarly, the fluorescence spectrum of the subsequent polymerization of f-NBEs ($n = 50$) was monitored (the second histogram in Fig. 5b), showing two emission peaks, centred at ~500 and ~550 nm. The latter peak is consistent with the macroscopic spectrum of the f-NBEs (Supplementary Fig. 49), indicating the generation of a block copolymer. The subsequent sequence copolymerization of f-COEs and f-NBEs exhibited a similar phenomenon (the third and fourth histograms in Fig. 5b). As the DP increased, photon counts did not increase notably, possibly because of self-quenching. To further prove the capability of controllable polymerization, the above method of regulating the turn-on/off of ROMP by EEF was applied to synthesize a polymer chain with the segment sequence of COE ($n = 20$) \rightarrow f-COE ($n = 1$) \rightarrow COE ($n = 20$) \rightarrow f-COE ($n = 1$) $\rightarrow \dots$, in which the fluorophores are far apart from each other to avoid self-quenching (Extended Data Fig. 3a). We measured the photon counts for every time that fluorescent monomer was inserted, and found that the emitted photons increased with several quantized steps with the increasing number of f-COEs (Extended Data Fig. 3b), which again verified the reliability of this regulation approach. Figure 5c,d provides $I-t$ curves of the copolymerization process with different n values, indicating precise control of the backbone structure. In combination with the regulation of chain conformation, polymerization dynamics and stereoregularity, online precise control of the DP and preparation of the block copolymer demonstrate the ability to completely manipulate the ROMP with single-molecule resolution.

Conclusions

In summary, we fully elucidated RCM and ROMP reaction mechanisms at the single-catalyst and single-event level on the basis of the sensitive graphene-based single-molecule electrical detection platform. For RCM, real-time reaction trajectories, including both productive and degenerate pathways, were accurately measured, deepening our understanding of metathesis reaction mechanisms. Moreover, the

constructive coupling between degenerate and productive metatheses provides a complete picture of the catalyst behaviour.

For ROMP, the EEF emerged as a powerful and efficient tool for regulating polymerization dynamics, polymer chain conformations, inserted monomer configurations and polymerization initiation/termination. A low EEF (0–0.5 V) enabled the manipulation of the equilibrium between polymerization and cyclodepolymerization, and facilitated the suppression of backbiting. A medium EEF (0.5–0.8 V) enabled the control of the stereoselectivity of inserted monomers and provided a simple and universal strategy for generating *Z*-isomers with high efficiency and selectivity. A high EEF (~1.0 V) terminated the polymerization and enabled control of the DP and precise synthesis of block copolymers. The utilization of this method to study other types of olefin metathesis, such as cross metathesis, ring-opening metathesis and acyclic diene metathesis, deserves further exploration. The application of electric fields to the reactions provides fertile ground for next-generation precise polymerization and organic synthesis.

Online content

Any methods, additional references, Nature Portfolio reporting summaries, source data, extended data, supplementary information, acknowledgements, peer review information; details of author contributions and competing interests; and statements of data and code availability are available at <https://doi.org/10.1038/s41565-024-01814-y>.

References

1. Vougioukalakis, G. C. & Grubbs, R. H. Ruthenium-based heterocyclic carbene-coordinated olefin metathesis catalysts. *Chem. Rev.* **110**, 1746–1787 (2010).
2. Trnka, T. M. & Grubbs, R. H. The development of L_2X_2RuCHR olefin metathesis catalysts: an organometallic success story. *Acc. Chem. Res.* **34**, 18–29 (2001).
3. Montgomery, T. P., Ahmed, T. S. & Grubbs, R. H. Stereoretentive olefin metathesis: an avenue to kinetic selectivity. *Angew. Chem. Int. Ed.* **56**, 11024–11036 (2017).
4. Fürstner, A. Olefin metathesis and beyond. *Angew. Chem. Int. Ed.* **39**, 3012–3043 (2000).
5. Grubbs, R. H. & Chang, S. Recent advances in olefin metathesis and its application in organic synthesis. *Tetrahedron* **54**, 4413–4450 (1998).
6. Nicolaou, K. C., Bulger, P. G. & Sarlah, D. Metathesis reactions in total synthesis. *Angew. Chem. Int. Ed.* **44**, 4490–4527 (2005).
7. Ogba, O. M., Warner, N. C., O'Leary, D. J. & Grubbs, R. H. Recent advances in ruthenium-based olefin metathesis. *Chem. Soc. Rev.* **47**, 4510–4544 (2018).
8. Becker, M. R., Watson, R. B. & Schindler, C. S. Beyond olefins: new metathesis directions for synthesis. *Chem. Soc. Rev.* **47**, 7867–7881 (2018).
9. Hilf, S. & Kilbinger, A. F. M. Functional end groups for polymers prepared using ring-opening metathesis polymerization. *Nat. Chem.* **1**, 537–546 (2009).
10. Mutlu, H., de Espinosa, L. M. & Meier, M. A. R. Acyclic diene metathesis: a versatile tool for the construction of defined polymer architectures. *Chem. Soc. Rev.* **40**, 1404–1445 (2011).
11. Sinclair, F., Alkattan, M., Prunet, J. & Shaver, M. P. Olefin cross metathesis and ring-closing metathesis in polymer chemistry. *Polym. Chem.* **8**, 3385–3398 (2017).
12. Ritter, T., Hejl, A., Wenzel, A. G., Funk, T. W. & Grubbs, R. H. A standard system of characterization for olefin metathesis catalysts. *Organometallics* **25**, 5740–5745 (2006).
13. Lee, J. B., Ott, K. C. & Grubbs, R. H. Kinetics and stereochemistry of the titanacyclobutane–titanaethylene interconversion. Investigation of a degenerate olefin metathesis reaction. *J. Am. Chem. Soc.* **104**, 7491–7496 (1982).

14. Tanaka, K., Tanaka, K., Takeo, H. & Matsumura, C. Intermediates for the degenerate and productive metathesis of propene elucidated by the metathesis reaction of (*Z*)-propene-1-*d*₁. *J. Am. Chem. Soc.* **109**, 2422–2425 (1987).
15. Stewart, I. C., Keitz, B. K., Kuhn, K. M., Thomas, R. M. & Grubbs, R. H. Nonproductive events in ring-closing metathesis using ruthenium catalysts. *J. Am. Chem. Soc.* **132**, 8534–8535 (2010).
16. Easter, Q. T. & Blum, S. A. Single turnover at molecular polymerization catalysts reveals spatiotemporally resolved reactions. *Angew. Chem. Int. Ed.* **56**, 13772–13775 (2017).
17. Easter, Q. T. & Blum, S. A. Evidence for dynamic chemical kinetics at individual molecular ruthenium catalysts. *Angew. Chem. Int. Ed.* **57**, 1572–1575 (2018).
18. Easter, Q. T., Garcia, A. I. V. & Blum, S. A. Single-polymer-particle growth kinetics with molecular catalyst speciation and single-turnover imaging. *ACS Catal.* **9**, 3375–3383 (2019).
19. Liu, C. et al. Single polymer growth dynamics. *Science* **358**, 352–355 (2017).
20. Ibrahim, I., Yu, M., Schrock, R. R. & Hoveyda, A. H. Highly *Z*- and enantioselective ring-opening/cross-metathesis reactions catalyzed by stereogenic-at-Mo adamantylimido complexes. *J. Am. Chem. Soc.* **131**, 3844–3845 (2009).
21. Flook, M. M., Jiang, A. J., Schrock, R. R., Müller, P. & Hoveyda, A. H. *Z*-selective olefin metathesis processes catalyzed by a molybdenum hexaisopropylterphenoxide monopyrrolide complex. *J. Am. Chem. Soc.* **131**, 7962–7963 (2009).
22. Jiang, A. J., Zhao, Y., Schrock, R. R. & Hoveyda, A. H. Highly *Z*-selective metathesis homocoupling of terminal olefins. *J. Am. Chem. Soc.* **131**, 16630–16631 (2009).
23. Koh, M. J., Nguyen, T. T., Zhang, H., Schrock, R. R. & Hoveyda, A. H. Direct synthesis of *Z*-alkenyl halides through catalytic cross-metathesis. *Nature* **531**, 459–465 (2016).
24. Koh, M. J. et al. Molybdenum chloride catalysts for *Z*-selective olefin metathesis reactions. *Nature* **542**, 80–85 (2017).
25. Torker, S., Müller, A. & Chen, P. Building stereoselectivity into a chemoselective ring-opening metathesis polymerization catalyst for alternating copolymerization. *Angew. Chem. Int. Ed.* **49**, 3762–3766 (2010).
26. Endo, K. & Grubbs, R. H. Chelated ruthenium catalysts for *Z*-selective olefin metathesis. *J. Am. Chem. Soc.* **133**, 8525–8527 (2011).
27. Keitz, B. K., Endo, K., Herbert, M. B. & Grubbs, R. H. *Z*-selective homodimerization of terminal olefins with a ruthenium metathesis catalyst. *J. Am. Chem. Soc.* **133**, 9686–9688 (2011).
28. Khan, R. K. M., Torker, S. & Hoveyda, A. H. Readily accessible and easily modifiable Ru-based catalysts for efficient and *Z*-selective ring-opening metathesis polymerization and ring-opening/cross-metathesis. *J. Am. Chem. Soc.* **135**, 10258–10261 (2013).
29. Khan, R. K. M., Torker, S. & Hoveyda, A. H. Reactivity and selectivity differences between catecholate and catechthiolate Ru complexes. Implications regarding design of stereoselective olefin metathesis catalysts. *J. Am. Chem. Soc.* **136**, 14337–14340 (2014).
30. Yang, C. et al. Unveiling the full reaction path of the Suzuki–Miyaura cross-coupling in a single-molecule junction. *Nat. Nanotechnol.* **16**, 1214–1223 (2021).
31. Zhang, A. et al. Catalytic cycle of formate dehydrogenase captured by single-molecule conductance. *Nat. Catal.* **6**, 266–275 (2023).
32. Yang, C. et al. Single-molecule electrical spectroscopy of organocatalysis. *Matter* **4**, 2874–2885 (2021).
33. Yang, C. et al. Real-time monitoring of reaction stereochemistry through single-molecule observations of chirality-induced spin selectivity. *Nat. Chem.* **15**, 972–979 (2023).
34. Zhang, L. et al. Electrochemical and electrostatic cleavage of alkoxyamines. *J. Am. Chem. Soc.* **140**, 766–774 (2018).
35. Yang, C. et al. Electric field-catalyzed single-molecule Diels–Alder reaction dynamics. *Sci. Adv.* **7**, eabf0689 (2021).
36. Guan, J. et al. Direct single-molecule dynamic detection of chemical reactions. *Sci. Adv.* **4**, eaar2177 (2018).
37. Guo, Y., Yang, C., Zhang, L. & Guo, X. Tunable interferometric effects between single-molecule Suzuki–Miyaura cross-couplings. *J. Am. Chem. Soc.* **145**, 6577–6584 (2023).
38. Guo, Y., Yang, C., Zhou, S., Liu, Z. & Guo, X. A single-molecule memristor based on an electric-field-driven dynamical structure reconfiguration. *Adv. Mater.* **34**, 2204827 (2022).
39. Chen, H. et al. Reactions in single-molecule junctions. *Nat. Rev. Mater.* **8**, 165–185 (2023).
40. Dief, E. M., Low, P. J., Díez-Pérez, I. & Darwish, N. Advances in single-molecule junctions as tools for chemical and biochemical analysis. *Nat. Chem.* **15**, 600–614 (2023).
41. Yang, C., Yang, C., Guo, Y., Feng, J. & Guo, X. Graphene–molecule–graphene single-molecule junctions to detect electronic reactions at the molecular scale. *Nat. Protoc.* **18**, 1958–1978 (2023).
42. Deiters, A. & Martin, S. F. Synthesis of oxygen- and nitrogen-containing heterocycles by ring-closing metathesis. *Chem. Rev.* **104**, 2199–2238 (2004).
43. Anderson, P. W. More is different. *Science* **177**, 393–396 (1972).
44. Strogatz, S. et al. Fifty years of ‘More is different’. *Nat. Rev. Phys.* **4**, 508–510 (2022).
45. Shaik, S., Ramanan, R., Danovich, D. & Mandal, D. Structure and reactivity/selectivity control by oriented-external electric fields. *Chem. Soc. Rev.* **47**, 5125–5145 (2018).
46. Shaik, S., Danovich, D., Joy, J., Wang, Z. & Stuyver, T. Electric-field mediated chemistry: uncovering and exploiting the potential of (oriented) electric fields to exert chemical catalysis and reaction control. *J. Am. Chem. Soc.* **142**, 12551–12562 (2020).
47. Shaik, S., Mandal, D. & Ramanan, R. Oriented electric fields as future smart reagents in chemistry. *Nat. Chem.* **8**, 1091–1098 (2016).
48. Dief, E. M. & Darwish, N. SARS-CoV-2 spike proteins react with Au and Si, are electrically conductive and denature at $3 \times 10^8 \text{ V m}^{-1}$: a surface bonding and a single-protein circuit study. *Chem. Sci.* **14**, 3428–3440 (2023).
49. Aragonès, A. C. et al. Electrostatic catalysis of a Diels–Alder reaction. *Nature* **531**, 88–91 (2016).
50. Monfette, S. & Fogg, D. E. Equilibrium ring-closing metathesis. *Chem. Rev.* **109**, 3783–3816 (2009).

Publisher’s note Springer Nature remains neutral with regard to jurisdictional claims in published maps and institutional affiliations.

Springer Nature or its licensor (e.g. a society or other partner) holds exclusive rights to this article under a publishing agreement with the author(s) or other rightsholder(s); author self-archiving of the accepted manuscript version of this article is solely governed by the terms of such publishing agreement and applicable law.

© The Author(s), under exclusive licence to Springer Nature Limited 2024

Methods

Molecular synthesis and characterization

All the details of the synthetic route and characterization of the products can be found in Supplementary Information.

Graphene point electrode array fabrication

Single-layer graphene was grown on a copper foil (25 μm thickness) pretreated with acetic acid through chemical vapour deposition. Poly(methylmethacrylate) (PMMA) 950 was then spin-coated on the copper-substrate graphene. After immersing the PMMA-graphene-copper layers in a FeCl_3 solution, the copper foil was etched away to form the PMMA-graphene layers. Then, the PMMA-supported graphene was rinsed with hydrochloric acid and deionized water and transferred to a silicon wafer with a layer of 3,000 \AA SiO_2 (1.5 cm \times 1.5 cm).

We deposited gold marks on the above silicon wafer via photolithography and thermal evaporation. Then, a graphene strip of 40 μm width was obtained using photolithography and oxygen plasma etching. On the basis of the designed masking pattern, the electrodes (80 \AA Cr and 800 \AA Au) were deposited on the graphene silicon wafer. After that, we deposited a layer of 400 \AA SiO_2 to prevent current leakage in the liquid phase.

On the basis of dashed-line lithography, the PMMA-graphene transistor was etched using electron-beam lithography to open windows on the PMMA film. Finally, nanogapped graphene point electrode arrays with carboxyl terminals were obtained using oxygen plasma etching and supplemental electrical burning.

Single-molecule device fabrication

2-Hydroxydiphenylphosphinylbenzene (10^{-3} mol l^{-1}), catalytic amounts of 4-dimethylaminopyridine and *N,N*-diisopropylethylamine, 1-ethyl-3-(3-dimethylaminopropyl) carbodiimide superdried CH_2Cl_2 solution and the above graphene device were added to a round-bottom flask to activate carboxyl terminals under anhydrous and anaerobic conditions. After 36 h, we rinsed the device with ultradried CH_2Cl_2 and tetrahydrofuran, and then put it into a tetrahydrofuran/ H_2O (10:1, v/v) solution with the molecular bridge (compound **6**, 10^{-4} mol l^{-1}) under anaerobic conditions for 24 h. After that, we removed the device, rinsed it with tetrahydrofuran, and dried it with N_2 .

Electrical characterization

The single-molecule device was placed in a vacuum cryogenic probe station (Lakeshore TTPX) during the experiments. The I - V curves were measured using an Agilent 4155C semiconductor parameter system. The output terminal of an UHFLI lock-in amplifier provided a constant bias for the I - t measurement. The current signal of the molecular loop was amplified using a DL121I amplifier and then recorded using a high-speed acquisition card (NIDAQ).

Single-catalyst-junction modification

The device containing a single HG2 junction was treated with 3-bromopropene to afford Ru-based alkylidene ($\text{Ru}=\text{CHCH}_2\text{Br}$). Then we added the device, amino fluorescent polystyrene beads and K_2CO_3 to a *N,N*-dimethylformamide solution to modify the catalyst terminus through nucleophilic substitution. After that, the device was removed, rinsed with *N,N*-dimethylformamide and dried with flowing N_2 . The successful modification of the single-catalyst junction was characterized by an optical method.

Theoretical calculation

All density functional theory computations were performed with Gaussian 09 software⁵¹. Geometry optimizations were performed at the B3LYP/BSI (BSI: def2SVP(Ru)-6-31G(d,p)(rest)) level⁵². Normal vibrational mode analysis at the same level confirmed that optimized structures were intermediates or transition states. Gibbs free energies were estimated by combining B3LYP-D3/def2TZVPP single-point

energies and Gibbs free-energy corrections from optimizations at the BSI level⁵³. Single points with solvent corrections were performed using the CPCM continuum model with toluene⁵⁴. The influence of the EEFs on the Gibbs free energies was explored by gradually increasing the EEF strength from 0 V nm^{-1} to 9.77 V nm^{-1} at the B3LYP-D3/def2TZVPP level.

The transport properties of molecular junctions were explored using the density functional theory combined with the non-equilibrium Green's function method, implemented in the ATOMISTIX TOOLKIT software package. The generalized gradient approximation in the Perdew-Burke-Ernzerhof form was used to describe the exchange-correlation energy. The PseudoDojo ONCV pseudopotential with medium basis set was adopted for the Ru atom, and the Trouiller-Martins non-local pseudopotential with double-zeta plus polarized basis set was adopted for the rest. A kinetic energy cut-off of 125 Hartree for the real-space grid and a $2 \times 2 \times 134$ Monkhorst-Pack k -point mesh were employed in the transport calculations.

Data availability

The data supporting the findings of this study are available within the paper and Supplementary Information. The datasets used in Supplementary Information are available online from the Zenodo repository at <https://doi.org/10.5281/zenodo.13777604>. Source data are provided with this paper.

References

1. Frisch, M. J. et al. *Gaussian 09* (Gaussian, 2013).
2. Stephens, P. J., Devlin, F. J., Chabalowski, C. F. & Frisch, M. J. Ab initio calculation of vibrational absorption and circular dichroism spectra using density functional force fields. *J. Phys. Chem.* **98**, 11623–11627 (1994).
3. Grimme, S., Ehrlich, S. & Goerigk, L. Effect of the damping function in dispersion corrected density functional theory. *J. Comput. Chem.* **32**, 1456–1465 (2011).
4. Barone, V. & Cossi, M. Quantum calculation of molecular energies and energy gradients in solution by a conductor solvent model. *J. Phys. Chem. A* **102**, 1995–2001 (1998).

Acknowledgements

We acknowledge primary financial support from the National Key R&D Program of China (2022YFE0128700 (to X.G.) and 2021YFA1200101 (to X.G.)), the National Natural Science Foundation of China (22150013 (to X.G.) and 21933001 (to X.G.)), the New Cornerstone Science Foundation through the XPLORER PRIZE (to X.G.), Beijing National Laboratory for Molecular Sciences (BNLMS-CXXM-202407 (to X.G.)), the Natural Science Foundation of Beijing (2222009 (to X.G.)), 'Frontiers Science Centre for New Organic Matter' at Nankai University (63181206 (to X.G.)), the Taishan Scholars Program of Shandong Province (tsqn202211012 (to Y.L.)), the China National Postdoctoral Program for Innovative Talents (BX20220014 (to C.Y.)), the National Natural Science Foundation of China (22303003 (to C.Y.)), the General Project of China Postdoctoral Science Foundation (2023M730049 (to C.Y.)), the China National Postdoctoral Program for Innovative Talents (BX20230024 (to Y.G.)) and the General Project of China Postdoctoral Science Foundation (2023M740065 (to Y.G.)).

Author contributions

X.G., Y.G. and C.Y. conceived and designed the experiments. Y.G. and C.Y. fabricated the devices and performed the device measurements. L.Z. and F.M. carried out the molecular synthesis. Y.L., Y.H., X.L. and J.H. built and analysed the computational model and performed the quantum transport calculation. X.G., F.M., Y.G., C.Y., Y.Y., K.N.H., Y.X. and C.J. analysed the data and wrote the paper. All the authors discussed the results and commented on the paper.

Competing interests

The authors declare no competing interests.

Additional information

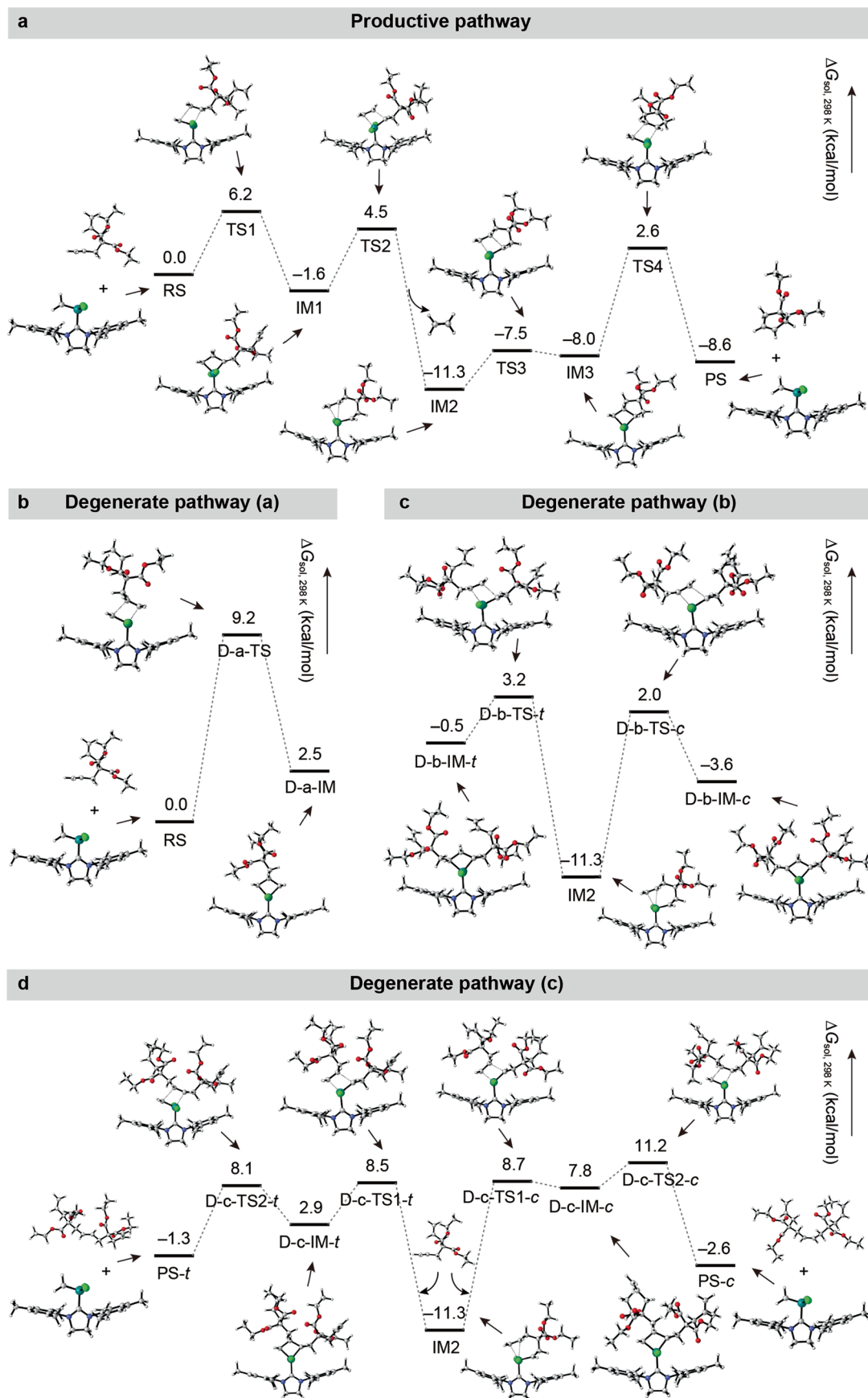
Extended data is available for this paper at <https://doi.org/10.1038/s41565-024-01814-y>.

Supplementary information The online version contains supplementary material available at <https://doi.org/10.1038/s41565-024-01814-y>.

Correspondence and requests for materials should be addressed to Fanyang Mo, Yanwei Li, Kendall N. Houk or Xuefeng Guo.

Peer review information *Nature Nanotechnology* thanks Nadim Darwish and Bingqian Xu for their contribution to the peer review of this work.

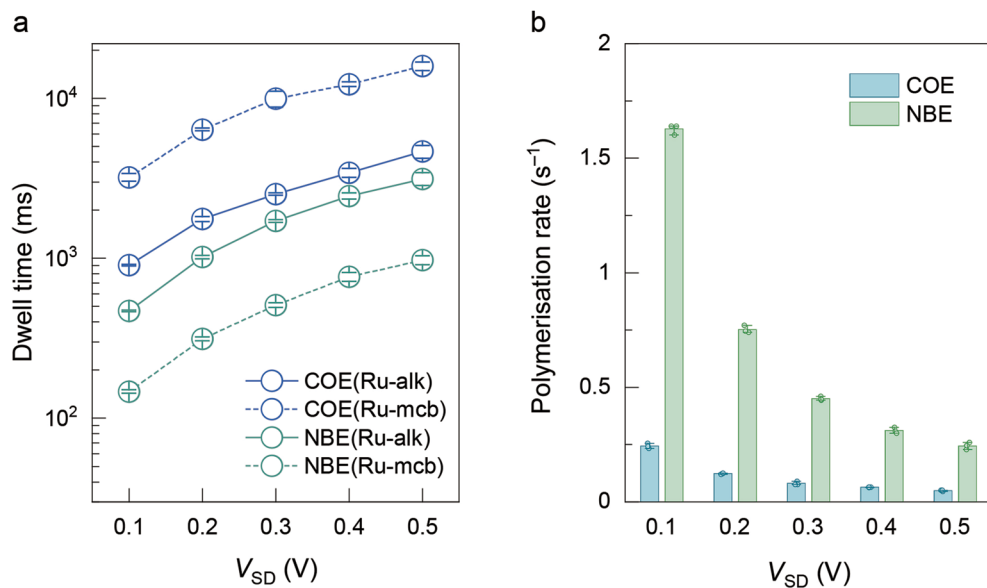
Reprints and permissions information is available at www.nature.com/reprints.



Extended Data Fig. 1 | See next page for caption.

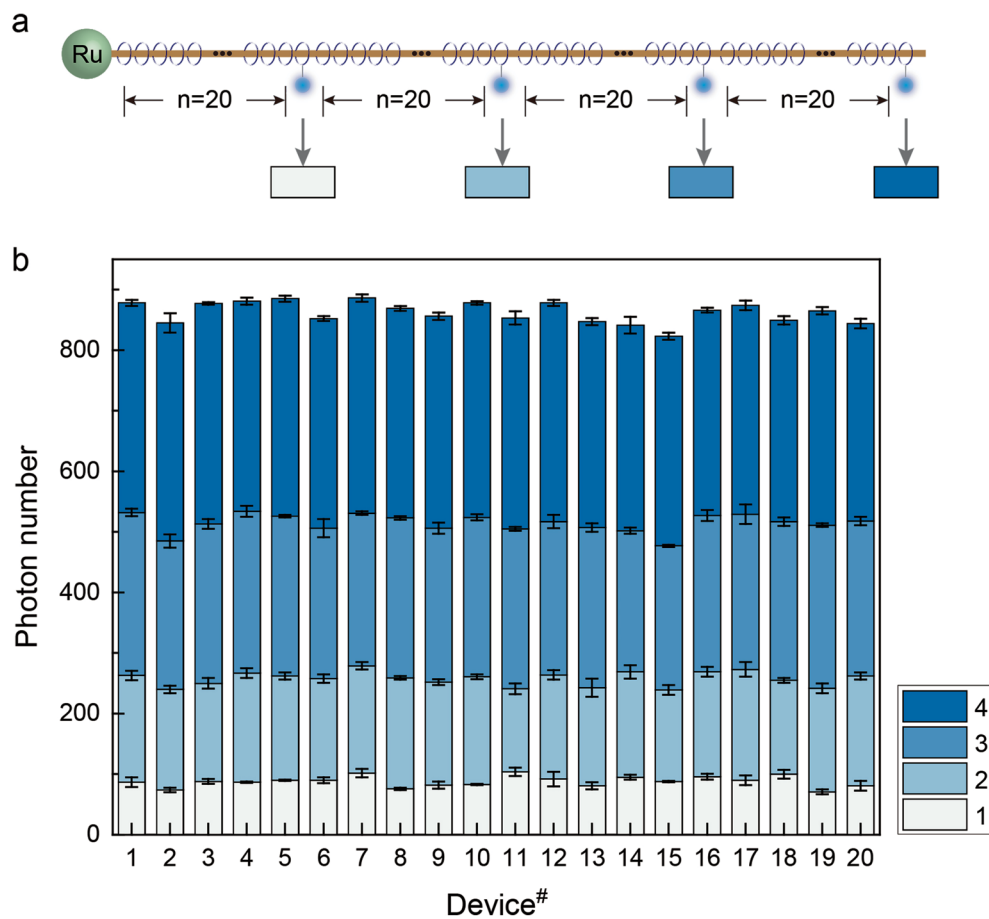
Extended Data Fig. 1 | Simulated potential energy profiles of different pathways in RCM. Gibbs free energies (kcal/mol) and intermediate structures are given in the figure. Computational studies were performed with B3LYP-D3/def2TZVPP//B3LYP/def2SVP(Ru) 6-31G(d,p)(C H O N Cl). Solvent = toluene; T = 298 K. **a.** Potential energy profile of the productive pathway. **b.** Potential energy profile of the degenerate pathway (a). **c.** Potential energy profile of the degenerate pathway (b). **d.** Potential energy profile of the degenerate pathway

(c). Abbreviations: **RS**, reactant state; **TS**, transition state; **IM**, intermediate; **PS**, productive state; **D**, degenerate; **a**, metathesis pathway (a); **b**, metathesis pathway (b); **c**, metathesis pathway (c); **t**, *trans*; **c**, *cis*. **RS** = complex 1 + substrate; **IM1** = complex 2; **IM2** = complex 3; **IM3** = complex 4; **PS** = complex 1 + product; **D-a-IM** = complex 5; **D-b-IM-t** = complex 6; **D-b-IM-c** = complex 7; **PS-t** = complex 1 + *trans*-product; **PS-c** = complex 1 + *cis*-product.



Extended Data Fig. 2 | Statistical dynamic information of ROMP. a. Dwell time of Ru-based alkylidene (solid line) and metallacyclobutane (dash line) in bias voltage-dependent measurements of ROMP using COE (blue line) and NBE (green line). Abbreviations: alk = alkylidene; mcb = metallacyclobutane. The error scales were derived from the statistics of three different devices ($n = 3$). Data are presented as mean \pm s.d. τ_{mcb} was longer than τ_{alk} in the polymerization of COE (for example, at $V_{SD} = 0.1$ V and COE concentration = 1×10^{-4} mol L $^{-1}$, $\tau_{mcb} = 3202.6 \pm 182.5$ ms, $\tau_{alk} = 906.5 \pm 10.4$ ms), indicating that the ring-opening process of

metallacyclobutane is the rate-determining step (RDS). As for NBE, the RDS is the formation of metallacyclobutane (for example, at $V_{SD} = 0.1$ V and NBE concentration = 1×10^{-4} mol L $^{-1}$, $\tau_{mcb} = 146.8 \pm 3.8$ ms, $\tau_{alk} = 468.0 \pm 5.2$ ms), which is consistent with the high ring strain energy of NBE. **b.** Polymerization rates in bias voltage-dependent measurements of ROMP using COE (blue bar) and NBE (green bar), demonstrating the high activity of NBE as the monomer in ROMP. The error scales were derived from the statistics of three different devices ($n = 3$). Data are presented as mean \pm s.d.



Extended Data Fig. 3 | Statistics of recorded photons of the polymer chain with different numbers of f-COE. a. Schematic of the polymer chain with the segment sequence of COE($n=20$) \rightarrow f-COE($n=1$) \rightarrow COE($n=20$) \rightarrow f-COE($n=1$) \rightarrow **b.** For 20 different devices, recorded photon numbers of the polymer chain

with different numbers of f-COE (1–4). For each device, the error scales were derived from the statistics of 3 independent tests ($n=3$). Data are presented as mean \pm s.d.